CrossMark

Reverberation Mapping of IC 4329A

Misty C. Bentz[1] , Christopher A. Onken[2] , Rachel Street[3] , and Monica Valluri[4]
[1] Department of Physics and Astronomy, Georgia State University, Atlanta, GA 30303, USA; bentz@astro.gsu.edu
[2] Research School of Astronomy and Astrophysics, Australian National University, Canberra, ACT 2611, Australia
[3] LCOGT, 6740 Cortona Drive, Suite 102, Goleta, CA 93117, USA
[4] Department of Astronomy, University of Michigan, Ann Arbor, MI, 48109, USA

Abstract

We present the results of a new reverberation mapping campaign for the broad-line active galactic nucleus (AGN) in the edge-on spiral IC 4329A. Monitoring of the optical continuum with V-band photometry and broad emission-line flux variability with moderate-resolution spectroscopy allowed emission-line light curves to be measured for Hβ, Hγ, and He II λ4686. We find a time delay of $16.3^{+2.6}_{-2.3}$ days for Hβ, a similar time delay of $16.0^{+4.8}_{-2.6}$ days for Hγ, and an unresolved time delay of $-0.6^{+3.9}_{-3.9}$ days for He II. The time delay for Hβ is consistent with the predicted value from the relationship between AGN luminosity and broad-line region radius, after correction for the ~2.4 mag of intrinsic extinction at 5100 Å. Combining the measured time delay for Hβ with the broad emission-line width and an adopted value of $\langle f \rangle = 4.8$, we find a central supermassive black hole mass of $M_{\rm BH} = 6.8^{+1.2}_{-1.1} \times 10^7 M_{\odot}$. Velocity-resolved time delays were measured across the broad Hβ emission-line profile and may be consistent with an "M"-like shape. Modeling of the full reverberation response of Hβ was able to provide only modest constraints on some parameters, but does exhibit agreement with the black hole mass and average time delay. The models also suggest that the AGN structure is misaligned by a large amount from the edge-on galaxy disk. This is consistent with expectations from the unified model of AGNs, in which broad emission lines are expected to be visible only for AGNs that are viewed at relatively face-on inclinations.

Unified Astronomy Thesaurus concepts: Reverberation mapping (2019); Seyfert galaxies (1447); Supermassive black holes (1663)

Supporting material: machine-readable table

1. Introduction

IC 4329A is a striking example of a broad-line active galactic nucleus (AGN) in an edge-on galaxy. Within the unified model for AGNs (Antonucci 1993), this would suggest that the rotation axis of the central supermassive black hole and the rotation axis of the galaxy disk are misaligned by a considerable angle. The misalignment of the galaxy and black hole are further supported by a ~50° difference between the position angle of the disk of IC 4329A and the position angle of extended radio emission from its nucleus (Schmitt et al. 1997; Nagar & Wilson 1999). AGN fueling events can torque the spin axis of the black hole (e.g., King & Pringle 2007) while black hole mergers can flip the spin axis (e.g., Lousto et al. 2016). With its membership within a loose group of galaxies inside the cluster Abell 3574 (Disney 1973; Wilson & Penston 1979; Abell et al. 1989) and close proximity to the giant lenticular IC 4329, it is possible that either of these scenarios may have occurred in IC 4329A. Furthermore, there is observational evidence for ongoing interactions between IC 4329 and IC 4329A (Read & Pietsch 1998), and IC 4329 is a shell galaxy (Malin & Carter 1983), which may be evidence of a past merger.

IC 4329A hosts a highly reddened AGN that is nevertheless apparently bright across the electromagnetic spectrum, which led Wilson & Penston (1979) to suggest that it is the *nearest*

quasar. Prior studies have concluded that the reddening arises from the AGN structure itself as well as the dust lane of the galaxy disk (Wolstencroft et al. 1995; Mehdipour & Costantini 2018). IC 4329A thus provides a rare opportunity to carry out detailed studies of the absorbing material around an accreting supermassive black hole, from the far-infrared through the X-rays (e.g., Mehdipour & Costantini 2018).

Currently lacking among the studies of IC 4329A, however, is an accurate constraint on the black hole mass. Reverberation mapping (Cackett et al. 2021), which uses spectrophotometric monitoring of an AGN to track changes in the continuum flux and the echoes of those changes in the broad emission lines, is often applied to bright and nearby broad-line AGNs and has resulted in a sample of ~70 black hole mass measurements to date in galaxies with $z \lesssim 0.4$ (Bentz & Katz 2015).

Strong flux variability in the nucleus of IC 4329A has been known for decades and an early reverberation mapping attempt was made by Winge et al. (1996). However, that early program was carried out before the typical size of the broad-line region (BLR) was well understood, and when estimates were about a factor of 10 too large. With an average (median) sampling rate of 8 (4) days, and utilizing the CTIO 2D-Frutti camera in the spectrograph—a photon-counting detector with significantly poorer performance than a CCD—the light curves were noisy, undersampled, and provided unreliable time delay measurements (Peterson et al. 2004).

We therefore undertook a new reverberation mapping campaign in the first half of 2022 with the aim of constraining the black hole mass of IC 4329A, and we describe the results of that program in this manuscript.

2. Observations

IC 4329A is an edge-on spiral galaxy located in the direction of Centaurus at R.A. $= 13^{h}49^{m}19\overset{s}{.}3$, decl. $= -30°18'34''$(J2000.0), and $z = 0.01605$. Based on fundamental plane studies (Hudson et al. 2001; Bernardi et al. 2002), the distance to the giant lenticular IC 4329 is $D = 59 \pm 9$ Mpc (Tully et al. 2009), which is consistent with the distance of $D = 69 \pm 18$ Mpc derived from observations of a Type 1a supernova (Stahl et al. 2021). IC 4329A is expected to have a similar distance as IC 4329 given the signatures of ongoing interactions between them.

2.1. Imaging

Photometric monitoring of IC 4329A was carried out with the Las Cumbres Observatory (LCO; Brown et al. 2013) 1.0 m telescope network under the program NSF-2022A-012 (PI: Bentz).[5] Observations began on 2022 February 3 (UT) and continued throughout the 2022A semester, ending on 2022 July 31. A 60 s V-band image was scheduled to occur every $\sim$8 hr using the Sinistro imaging cameras, providing a $26\overset{'}{.}5 \times 26\overset{'}{.}5$ field of view and an angular scale of $0\overset{''}{.}389$ pix^{-1}.

Over the course of the semester, a total of 374 images were acquired from the LCO facilities at three sites—164 from Cerro Tololo Interamerican Observatory (CTIO), 138 from the South African Astronomical Observatory (SAAO), and 72 from Siding Spring Observatory (SSO)—with a median (average) time sampling of 0.35 (0.47) days. All observations were reduced by the LCO pipeline (McCully et al. 2018), which applies typical CCD corrections using bias, flat, and dark frames, and the fully reduced images were downloaded from the LCO archive.[6]

The V band covers a relatively emission-line-free region of the spectral energy distribution for nearby AGNs, and is therefore an excellent probe of the continuum variability. However, nearby AGNs live in optically bright and spatially resolved nearby galaxies. We therefore relied on image subtraction methods (Alard & Lupton 1998; Alard 2000) to isolate and measure the variable flux in the nucleus of IC 4329A. Image subtraction has the advantage over aperture photometry in that non-variable flux sources, such as the host galaxy, are removed in the processing. The removal of the host galaxy results in a reduction of the noise caused by variable seeing affecting the amount of light within a fixed aperture, and it also removes the damping effect on the intrinsic variability that is caused by a large constant-flux offset. Because of the advantages, image subtraction methods are commonly applied in studies of transients and other time domain phenomena, including microlensing (Udalski et al. 2008, 2015), supernovae (Riess et al. 2001; Miknaitis et al. 2007; Melinder et al. 2008), tidal disruption events (Holoien et al. 2016; Brown et al. 2018), as well as AGN variability (Fausnaugh et al. 2016; Grier et al. 2017; Bentz et al. 2021a).

We first registered all images to a common reference grid with the algorithm of Siverd et al. (2012). Using the algorithms of Alard & Lupton (1998) and Alard (2000), we then built a reference image (Figure 1) from the subset of frames collected at CTIO with the lowest backgrounds and best seeing. For each observation collected throughout the semester, we then convolved the reference frame to match the image, subtracted the convolved reference from the observed image, and

measured the residual counts at the position of the AGN using an aperture with a radius of 9 pixels.

To convert the residual counts to calibrated fluxes, we carried out a 2D surface brightness decomposition of the reference frame. Using Galfit (Peng et al. 2002, 2010), we modeled the separate photometric components of IC 4329A and the nearby lenticular IC 4329. A model of the point-spread function (PSF) of the image was generated by fitting four Gaussian profiles to a bright and isolated field star. For each of the Gaussian profiles, we allowed the first mode of the Fourier perturbation series to vary in an effort to better account for slight asymmetries in the PSF shape. The resultant PSF model image was then used to model the AGN as well as several field stars with cataloged V-band magnitudes. An exponential profile with a radial truncation was used to model the edge-on galaxy disk and its extinguishing dust lane, while Sérsic profiles modeled the bulge and companion galaxy. Finally, the background sky was modeled with a tilted plane to allow for gradients in both the x and y directions. The final zero-point of the flux calibration was set by minimizing the difference between the fitted magnitudes of the field stars and their reported magnitudes in the AAVSO Photometric All Sky Survey catalog (Henden & Munari 2014). Once the models were optimized, the final modeled AGN magnitude was combined with the residual counts to determine the calibrated fluxes for each V-band measurement throughout the campaign.

As we found in our previous monitoring study of NGC 3783 (Bentz et al. 2021a), the images acquired from the three Southern LCO 1 m sites have slight photometric offsets between them. We identified observations that were collected close in time (<0.5 day) from CTIO and SSO, as well as from CTIO and SAAO. We then determined and applied the slight linear scaling needed to bring the SAAO and SSO measurements into agreement with the CTIO measurements, as the CTIO data set was used to build the reference frame for image subtraction and to determine the AGN mean magnitude.

Previous work has found that the flux uncertainties associated with image subtraction methods are often underestimated (Zebrun et al. 2001; Hartman et al. 2005). We therefore followed the basic procedure outlined by Hartman et al. (2004) and examined the residual counts left behind by non-varying field stars, identifying the factor by which the uncertainties needed to be expanded to account for the scatter in residual flux from stars of a similar magnitude as the AGN. The uncertainties on the AGN fluxes were then inflated by this scale factor.

Finally, over the course of $\sim$2 months in the middle of the campaign, the fluxes measured for the AGN varied strongly and extremely rapidly from observation to observation. Inspection of the images acquired during these dates found that some of this rapid variability coincided with bright and uneven backgrounds in the images that could not be approximated with a simple gradient. Many of these dates also coincide with the Full Moon, and the uneven backgrounds appear to be associated with the reflection of moonlight within the domes. Rather than discard all of these frames and accept gaps of several days in the middle of the light curve, we instead discarded only the most egregious frames and binned all the remaining measurements with a bin size of 1.5 days. This bin size was determined through testing to provide a reasonable compromise between retaining temporal sampling and decreasing wild flux variations that cause difficulties in the time delay analysis.
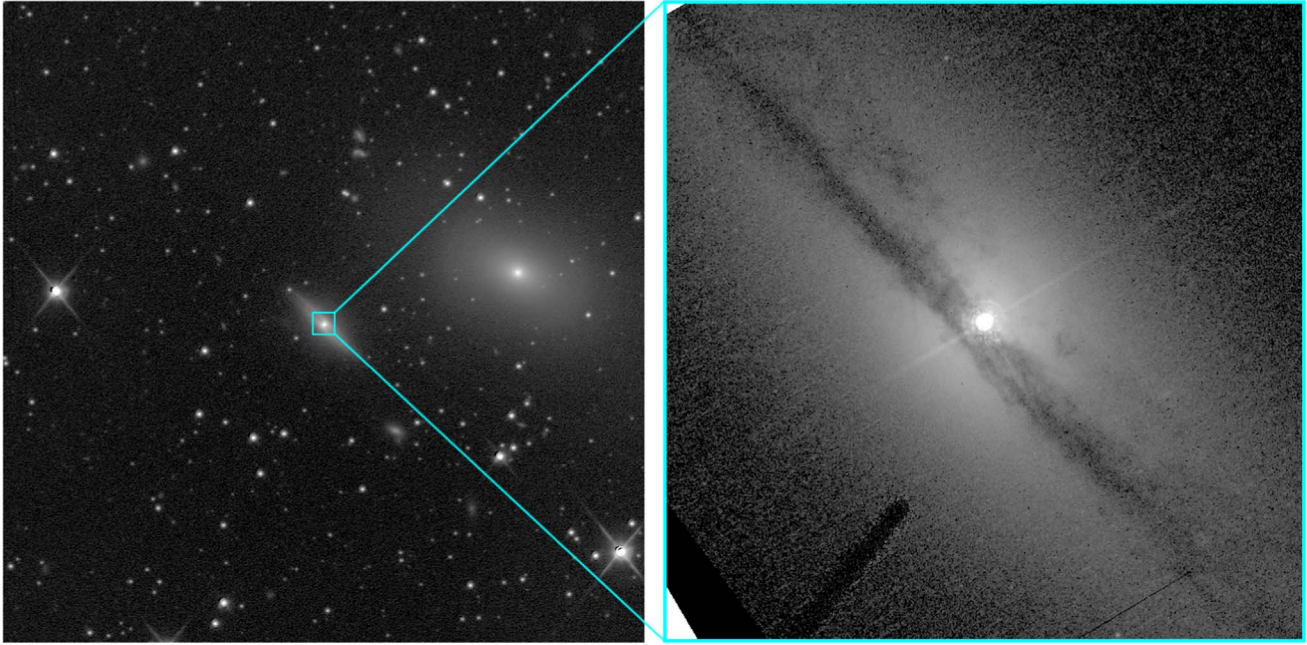

Figure 1. Left: the central $10' \times 10'$ of the reference image of IC 4329A, centered on the AGN. The image is oriented with north up and east to the left, and the giant lenticular galaxy IC 4329 is visible to the west of IC 4329A. Right: Hubble Space Telescope image of the central $20'' \times 20''$ in IC 4329A, highlighting the bright central AGN peeking over the dust lane in the disk of the galaxy.

In Figure 2 we display the final calibrated and binned V-band light curve of IC 4329A, along with a plot of the residuals from a field star of similar brightness for comparison.

2.2. Spectroscopy

Spectroscopic monitoring with the FLOYDS spectrographs on the 2.0 m Faulkes Telescopes North and South was carried out under programs NSF-2022A-012 and ANU-2022A-002. The FLOYDS spectrographs are cross-dispersed instruments providing wavelength coverage of 540–1000 nm with a dispersion of $3.51 \, \text{Å} \, \text{pix}^{-1}$ in the first order, and wavelength coverage of 320–570 nm with a dispersion of $1.74 \, \text{Å} \, \text{pix}^{-1}$ in the second order. Observations began on 2022 March 7 and were scheduled every ~24 hr through 2022 July 31. Over the course of the semester, 45 spectra (23 from FTN and 22 from FTS) were acquired with a median (average) time sampling of 2.0 (3.2) days.

Each observation consisted of a 1200 s spectrum of IC 4329A through the $6\rlap{.}''0$ slit, with an arc lamp and flat field taken at the same position. On several visits, we also acquired a 60 s spectrum of the nearby A0 spectrophotometric standard star CD-32 9927 (Hamuy et al. 1992, 1994) through the $6\rlap{.}''0$ slit.

The LCO pipeline splits the two spectral orders into separate images, after which it rectifies each order and applies typical CCD reductions, including biases, flats, and darks as well as an initial wavelength and flux calibration based on cataloged wavelength and sensitivity functions. We began our custom processing with the 2D flux- and wavelength-calibrated frames produced by the pipeline, focusing on the second-order (blue) spectra with their higher spectral resolution and coverage of the Hβ and [O III] emission. Working in IRAF[7] we detected and
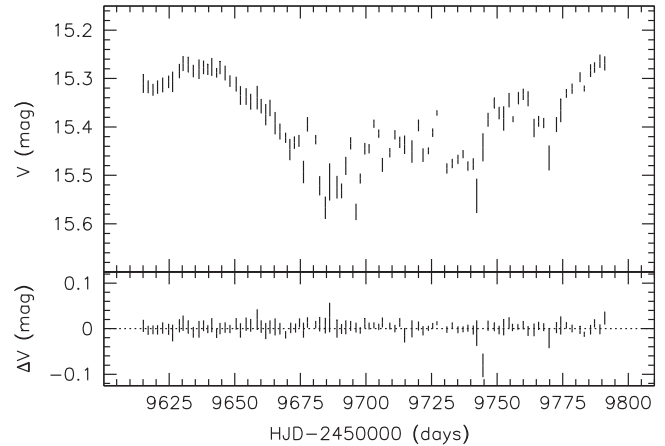

Figure 2. Top: final calibrated and binned V-band light curve of IC 4329A. Bottom: magnitude residuals for a non-varying $V = 15.3$ mag field star.

cleaned the science frames of cosmic rays and then extracted 1D spectra of IC 4329A, the standard star, and the arc lamps with a 10 pixel extraction width (corresponding to an angular width of $3\rlap{.}''37$). We then used the arc lamp spectra to improve the wavelength calibration for each observation, and finally adopted and applied a common dispersion of $1.6 \, \text{Å} \, \text{pix}^{-1}$.

For the visits that included an observation of the standard star, we fit a low-order polynomial to the standard star spectrum and compared this to the tabulated spectrum of Hamuy et al. (1992, 1994). We then determined the scaling needed to match the tabulated standard spectrum, and applied this scaling to the spectrum of IC 4329A that was collected during the same visit. Given the lack of standard star observations on several nights and the non-photometric conditions under which many spectra were acquired, we were unable to improve the flux calibration of all the observations of IC 4329A in this way. We instead focused on determining the

---

[7] IRAF is distributed by the National Optical Astronomy Observatories, which are operated by the Association of Universities for Research in Astronomy, Inc., under cooperative agreement with the National Science Foundation.
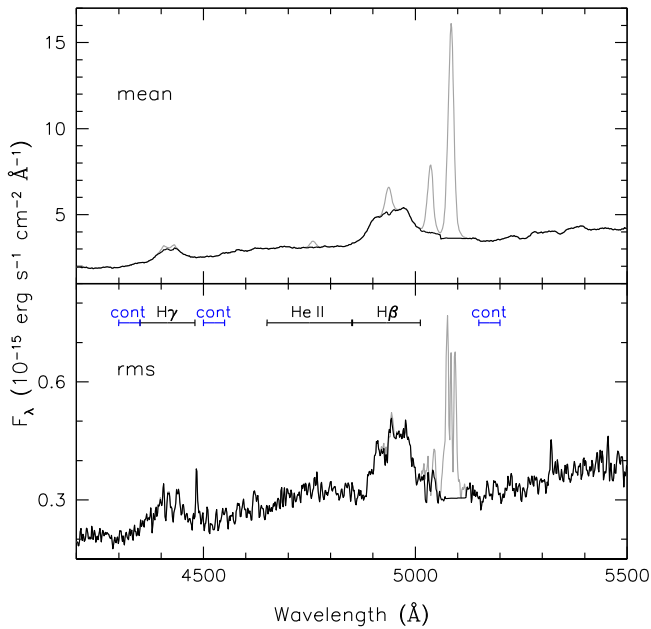
Figure 3. Mean (top) and rms (bottom) of the IC 4329A spectra collected throughout the monitoring program. Integration limits for the broad emission lines are displayed as the horizontal bars, and the adopted continuum windows are displayed as the blue horizontal bars. The gray (black) lines show the spectra before (after) narrow-line subtraction.

absolute calibration of the [O III] $\lambda 5007$ Å emission line from photometric nights that included observations of both IC 4329A and CD-32 9927, finding $F(5007) = (2.34 \pm 0.13) \times 10^{-13}$ erg s^{-1} cm^{-2}. This value agrees well with the flux reported by Morris & Ward (1988) of $F(5007) = 2.4 \times 10^{-13}$ erg s^{-1} cm^{-2} and is slightly higher, but within 2σ, of the value reported by Winge et al. (1996) of $F(5007) = (1.87 \pm 0.22) \times 10^{-13}$ erg s^{-1} cm^{-2}.

Finally, we applied the spectral scaling method of van Groningen & Wanders (1992) to all of the individual spectra of IC 4329A, focusing on the [O III] doublet. The [O III] emission lines are not variable on the timescales probed within a single observing semester (Peterson et al. 2013) and may therefore be used as an internal calibration *lamp*. The algorithm applies small shifts and smoothing to minimize the differences between an observed spectrum and a reference spectrum (created by averaging together several of the best-quality spectra), thus correcting for residual wavelength shifts, offsets in the flux calibration relative to the value of $F(5007)$ that we determined above, and differences in the spectral resolution arising from variable seeing throughout the campaign.

In Figure 3 we display the mean and rms of the blue spectra of IC 4329A collected throughout the monitoring campaign. Strong variability is evident in the rms of the broad Balmer lines Hβ and Hγ as well as the He II $\lambda 4686$ Å line.

3. Analysis

3.1. Emission-line Light Curves and Time Delays

With our final scaled spectra, we were able to measure the integrated fluxes of the broad emission lines and create their light curves. We began by setting a local linear continuum based on line-free regions on either side of a broad emission line of interest, and then integrating all of the flux above the continuum within a specified window. Thus, the emission-line fluxes include the narrow-line components as constant-flux

offsets. While simplistic, this method avoids inserting additional uncertainties into the measurements and has been shown to work well when applied to high signal-to-noise spectra with relatively unblended emission lines (e.g., Peterson et al. 2004; Bentz et al. 2009b).

We provide the light curves in Table 1 and plot them in Figure 4, while we tabulate several useful statistics for each light curve in Table 2. For each spectral feature listed in Column (1), we give the number of measurements in Column (2), and the average and median temporal sampling, respectively, in Columns (3) and (4). Column (5) lists the mean flux and standard deviation, while Column (6) lists the mean fractional error. Column (7) gives the noise-corrected fractional variation, which is computed as

$$F_{\mathrm{var}} = \frac{\sqrt{\sigma^2 - \delta^2}}{\langle F \rangle}, \qquad (1)$$

where σ^2 is the variance of the fluxes, δ^2 is their mean-square uncertainty, and $\langle F \rangle$ is the mean flux. Finally, Column (8) lists the ratio of the maximum to the minimum flux in the light curve.

To measure the time delays between the emission-line light curves and the *V*-band light curve, we began by employing the interpolated cross-correlation function (ICCF) method of Gaskell & Sparke (1986); Gaskell & Peterson (1987) with the modifications of White & Peterson (1994). The ICCF method determines the cross-correlation function twice, first when the continuum light curve is interpolated and then when the emission-line light curve is interpolated, and then averages the two together. These averaged CCFs are displayed in the panels on the right side of Figure 4.

From the CCF, the time delay may be reported as τ_{peak}, the time lag at which the peak (r_{max}) of the CCF occurs, or τ_{cent}, the centroid of the CCF above some value (usually $0.8 r_{\mathrm{max}}$). We employ the flux randomization/random subset sampling (FR/RSS) method (Peterson et al. 1998, 2004) to quantify the uncertainties on the time delays. In short, the flux randomization accounts for the effects of the measurement uncertainties on the derived time delay, and the random subset sampling accounts for the inclusion or exclusion of any specific data point in the analysis. The FR/RSS method is run in a Monte Carlo fashion, carrying out a large number of realizations to build up a distribution of CCF measurements. We ran 1000 realizations of the FR/RSS method and adopted the median and 68% confidence interval of the distributions to define the time delays, τ_{cent} and τ_{peak}, and their uncertainties, which are tabulated in Table 3.

We also investigated the time delays with JAVELIN (Zu et al. 2011), which fits a damped random walk model to the continuum light curve and then determines the best parameters for a top-hat function with which to delay and smooth the continuum light curve to match the emission-line light curve. JAVELIN is capable of fitting multiple emission lines at the same time, and it assesses the uncertainties on the reported time delay through a Bayesian Markov Chain Monte Carlo method. We fit all of the emission lines simultaneously, as well as individually, and found that both methods recovered time delays that agree fairly well. We list the time delays, denoted as τ_{jav}, from fitting all three emission lines simultaneously in Table 3.

<div align="center">

Table 1
Continuum and Emission-line Light Curves

</div>

Continuum			Emission Lines						
	V			Hβ		Hγ		He II	
HJD	F_λ	σ_F	HJD	F	σ_F	F	σ_F	F	σ_F
9615.1116	2.666	0.046	9646.0925	3.124	0.031	0.700	0.025	0.746	0.031
9616.9787	2.651	0.032	9647.0745	3.075	0.029	0.680	0.023	0.747	0.029
9618.7941	2.636	0.031	9649.1018	3.020	0.033	0.639	0.027	0.584	0.034
9620.5635	2.650	0.034	9651.0854	3.155	0.028	0.711	0.022	0.715	0.028
9622.5523	2.660	0.038	9657.0617	3.022	0.032	0.685	0.030	0.521	0.036

Note. Heliocentric Julian dates are provided as HJD-2450000 (days). V-band flux densities have units of 10^{-15} erg s^{-1} cm^{-2} Å^{-1} while emission-line fluxes have units of 10^{-13} erg s^{-1} cm^{-2}. Table 1 is published in its entirety in machine-readable format. A portion is shown here for guidance regarding its form and content.

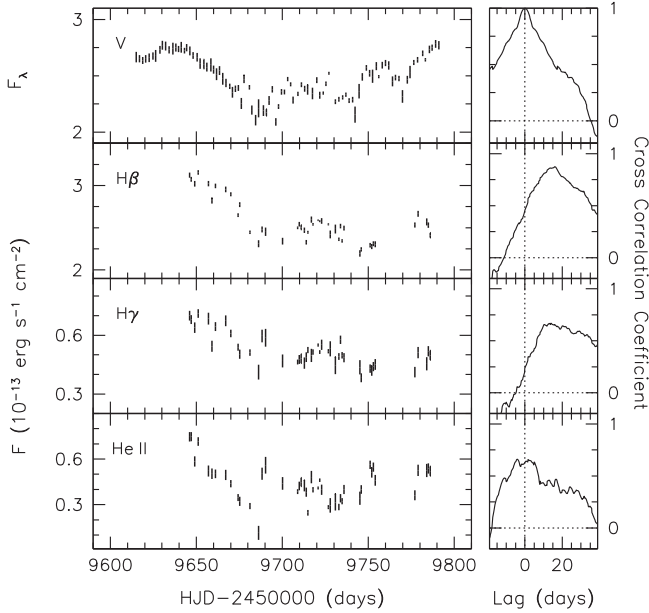(This table is available in its entirety in machine-readable form.)

Figure 4. Left: V-band and emission-line light curves for IC 4329A. Flux densities are in units of 10^{-15} erg s^{-1} cm^{-2} Å^{-1}, and integrated fluxes are in units of 10^{-13} erg s^{-1} cm^{-2}. Right: cross-correlation functions relative to the V-band light curve (for the V-band light curve, this is the autocorrelation function).

3.2. Line Width Measurements

The widths and shapes of the broad emission lines provide information on the kinematics of the line-emitting gas, and are generally reported as the velocity dispersion of the line profile, σ_{line}, and the FWHM. Previous reverberation studies have often reported different broad-line widths when measured in the mean versus the rms spectrum (for a compilation, see Bentz & Katz 2015), with the rms spectrum crucially providing a measure of the kinematics of the reverberating gas. Furthermore, the rms spectrum suppresses the non-variable narrow-line contribution.

While the rms spectrum suppresses the narrow-line contribution, the narrow lines must be fitted and removed from the mean spectrum before measuring the broad-line widths. We used the [O III] λ5007 line as a template that was shifted and scaled to match the other narrow lines in the relevant portions of the spectrum—[O III] λ4959 and λ4363, and the narrow components of Hβ, He II, and Hγ—and then subtracted. In Figure 3 we display the mean and rms spectra before and after

narrow-line subtraction in gray and black, respectively. As expected, the rms profiles of the broad emission lines are relatively unaffected by the narrow-line subtraction.

To determine the uncertainties on the line widths, we employed a bootstrap sampling method that selects a random subset of spectra, creates a mean and rms spectrum, and then measures the line width directly from the data by fitting a local linear continuum under each emission line and then constraining the width of the flux in excess of the continuum. We ran 1000 realizations of the method and built up a distribution of σ_{line} and FWHM measurements, from which we report the median and 68% confidence interval as the measurement and its uncertainty, respectively. As expected, the line widths in the mean spectrum increased after narrow-line subtraction had been applied (especially FWHM), while the line widths remained the same in the rms spectrum before and after narrow-line subtraction. We report both the FWHM and σ_{line} for the mean and rms spectra, after narrow-line subtraction, in Table 3.

All reported line widths were corrected for the resolution of the spectrograph by assuming

$$\Delta\lambda_{\text{obs}}^2 \approx \Delta\lambda_{\text{true}}^2 + \Delta\lambda_{\text{disp}}^2, \qquad (2)$$

where $\Delta\lambda_{\text{obs}}$ is the measured width of an emission line and $\Delta\lambda_{\text{disp}}$ is the broadening caused by the instrument. We estimated $\Delta\lambda_{\text{true}}$, the intrinsic line width, by adopting the width of [O III] λ5007 Å measured by Whittle (1992) through a small spectrograph slit and at high resolution, FWHM = 550 km s^{-1}. Combining $\Delta\lambda_{\text{true}}$ with $\Delta\lambda_{\text{obs}}$, we found $\Delta\lambda_{\text{disp}} = 13.9$ Å.

4. Discussion

4.1. Radius versus Luminosity

The mean and rms flux at $5100 \times (1 + z)$ Å throughout the monitoring campaign was measured to be $F_\lambda(5100) = (3.49 \pm 0.30) \times 10^{-15}$ erg s^{-1} cm^{-2} Å^{-1}. However, with the large spectroscopic aperture employed, a significant fraction of this flux is expected to come from stars in the host galaxy rather than the AGN itself. IC 4329A was observed with the Hubble Space Telescope Advanced Camera for Surveys High Resolution Channel through the F550M filter in 2006 as part of program GO-10516 (see Figure 1). Bentz et al. (2009a) report a 2D surface brightness decomposition of the image, from which we determined the host galaxy contribution through the

Table 2
Light-curve Statistics

Time Series (1)	N (2)	$\langle \Delta T \rangle$ (days) (3)	ΔT_{med} (days) (4)	$\langle F \rangle$ (5)	$\langle \sigma_F/F \rangle$ (6)	F_{var} (7)	R_{max} (8)
V	91	2.0 ± 0.4	1.9	2.49 ± 0.18	0.014	0.07	1.332 ± 0.027
Hβ	45	3.2 ± 3.9	2.0	2.57 ± 0.25	0.011	0.10	1.436 ± 0.028
Hγ	45	3.2 ± 3.9	2.0	0.52 ± 0.08	0.049	0.15	1.859 ± 0.126
He II	45	3.2 ± 3.9	2.0	0.44 ± 0.13	0.079	0.28	6.553 ± 2.661

Note. V-band flux densities have units of 10^{-15} erg s^{-1} cm^{-2} Å^{-1} while emission-line fluxes have units of 10^{-13} erg s^{-1} cm^{-2}.

spectroscopic aperture utilized in this work, $F_{\lambda,gal}(5100) = (2.15 \pm 0.22) \times 10^{-15}$ erg s^{-1} cm^{-2} Å^{-1}.

Removing the starlight contribution to the flux measured at $5100 \times (1 + z)$ Å, correcting for Galactic absorption ($A_B = 0.21$ mag, Schlafly & Finkbeiner 2011), and assuming a distance of $D = 59 \pm 9$ Mpc (as measured for IC 4329, Tully et al. 2009), we find an average nuclear luminosity of $\log \lambda L_\lambda(5100) = 42.53 \pm 0.15$ $L_\odot$ for IC 4329A during this monitoring campaign. Based on the relationship between BLR radius and AGN luminosity for local Seyferts (Bentz et al. 2013), we would thus predict an Hβ time delay of $\sim$6 days.

However, the observed nuclear luminosity is likely a severe underestimate because of the intrinsic extinction along our line of sight to the center of IC 4329A. Mehdipour & Costantini (2018) analyzed the spectral energy distribution of IC 4329A from the X-rays through the far-infrared, finding that the internal extinction was best described by a flat or gray extinction curve, similar to that described by Czerny et al. (2004), with $E(B - V) = 1.0 \pm 0.1$ mag. These results suggest that the intrinsic AGN flux at $5100 \times (1 + z)$ Å is $\sim$9.5$\times$ larger than the observed flux. Adjusting the nuclear luminosity by this factor then predicts an Hβ time delay of $\sim$18 days, in good agreement with the measurements we present here given the uncertainties involved in correcting internal extinction.

4.2. Black Hole Mass

The time delay for a broad emission line (τ) gives a measure of the light-crossing time and thus the physical size of the emission-line region, while the width of the line (V) provides a constraint on the line-of-sight velocity of the gas in the region. The two may be combined to derive the black hole mass as

$$M_{BH} = f \frac{c\tau V^2}{G}, \tag{3}$$

where c is the speed of light, and G is the gravitational constant. The scale factor f is an order unity term that includes the detailed geometry and kinematics of the BLR as well as the inclination angle at which the AGN system is viewed.

Historically, it has been difficult to constrain the BLR structure and kinematics for most AGNs that have been studied with reverberation mapping. Thus, a population-average scale factor, $\langle f \rangle$, is generally adopted to bring the sample of reverberation-based masses into general agreement with samples of black hole masses from dynamical modeling through comparison of their $M_{BH}-\sigma_\star$ relationships. Previous studies have found values of $\langle f \rangle = 2.8$–5.5, depending on the details of the adopted samples and the fitting method (Onken et al. 2004; Graham et al. 2011; Park et al. 2012; Grier et al. 2013a; Batiste et al. 2017). These values of $\langle f \rangle$ are appropriate for time delays given by τ_{cent} and line widths given by

σ_{line}(rms), the combination of measurements that has been shown to provide the smallest scatter among black hole masses derived from multiple reverberation experiments targeting the same AGN (Peterson et al. 2004). We note, however, that while adopting $\langle f \rangle$ minimizes any bias in a sample of reverberation masses, it also means that the reverberation mass for any single AGN may be uncertain by a factor of a few. In particular, the inclinations of individual AGNs to our line of sight are expected to be random, and the analysis of Williams et al. (2018) suggests that inclination plays a significant role in the variance of individual f values determined for different AGNs (see also, e.g., Collin et al. 2006).

Here we adopt $\langle f \rangle = 4.8$ from Batiste et al. (2017) because of their careful assessment of galaxy morphology on the determination of $\sigma_\star$ among the AGN sample. Combined with τ_{cent} and σ_{line}(rms) for Hβ, we find $M_{BH} = 6.8^{+1.2}_{-1.1} \times 10^7 M_\odot$. We find a similar mass with slightly larger uncertainties, $M_{BH} = 5.5^{+1.9}_{-1.2} \times 10^7 M_\odot$, using the measurements of Hγ and adopting the same value of $\langle f \rangle$.

The $M_{BH}-\sigma_\star$ relationship is commonly used to estimate black hole masses in galaxies, although estimates for the black hole mass in IC 4329A based on the $M_{BH}-\sigma_\star$ relationship are likely to be biased somewhat high because of the rotational contribution of the edge-on galaxy disk to $\sigma_\star$. Using the $M_{BH}-\sigma_\star$ relationship of Tremaine et al. (2002); Markowitz (2009) estimated $M_{BH} = 2^{+2}_{-1} \times 10^8 M_\odot$ for IC 4329A, which is indeed somewhat higher than the reverberation mass we present here. Markowitz (2009) also estimated the black hole mass using the McHardy et al. (2006) relationship between bolometric luminosity, black hole mass, and X-ray power spectral density break, finding $M_{BH} = 1.3^{+1.0}_{-0.3} \times 10^8 M_\odot$. Markowitz (2009) assumed a luminosity distance of 78.6 Mpc when calculating the bolometric luminosity, so adopting the measured distance to IC 4329 of $D = 59$ Mpc decreases the predicted mass by $\sim$23%, bringing it into better agreement with the reverberation mass. Finally, Ponti et al. (2012) explored the relationship between X-ray excess variance and M_{BH}, using the reverberation sample to define a scaling relationship between the two. With this scaling relationship, they predict $M_{BH} = 2.1^{+1.3}_{-0.8} \times 10^8 M_\odot$ for IC 4329A, although we note that they adopted a mass estimate for IC 4329A based on $M_{BH}-\sigma_\star$ and included it as one of the few black holes with $M_{BH} > 10^8 M_\odot$ in the reverberation sample that defined the scaling relationship.

4.3. Velocity-resolved Time Delays

While a population-average scale factor $\langle f \rangle$ is generally adopted for reverberation masses, it was understood from the initial development of reverberation mapping that the response as a function of velocity across an emission line would provide information on the overall geometry and kinematics of the BLR

Table 3
Emission-line Time Lags and Widths

Line	τ_{cent} (days)	τ_{peak} (days)	τ_{jav} (days)	Mean FWHM (km s^{-1})	Mean σ_{line} (km s^{-1})	rms FWHM (km s^{-1})	rms σ_{line} (km s^{-1})
Hβ	$16.33^{+2.59}_{-2.28}$	$16.00^{+0.50}_{-2.75}$	$16.09^{+0.54}_{-1.26}$	6944 ± 51	2247 ± 8	4789 ± 869	2112 ± 93
Hγ	$16.04^{+4.83}_{-2.60}$	$13.25^{+4.25}_{-2.75}$	$15.48^{+0.96}_{-2.23}$	4176 ± 162	1703 ± 61	4607 ± 948	1908 ± 149
He II	$-0.59^{+3.87}_{-3.85}$	$0.25^{+4.75}_{-4.75}$	$-1.37^{+2.04}_{-2.37}$	$\cdots$	$\cdots$	8099 ± 1574	3334 ± 134

Note. Reported time lags are in the observer's frame, while line widths are in the rest frame.

gas (Blandford & McKee 1982). Mapping the BLR via reverberation would then allow the black hole mass to be directly constrained, without reliance on a scale factor. Initial attempts to constrain velocity-resolved time delays were generally hampered by observational uncertainties and systematics, but more recently there have been a growing number of successes (e.g., Bentz et al. 2008; Denney et al. 2009; Grier et al. 2013b; Fausnaugh et al. 2017; Brotherton et al. 2020; Oknyansky et al. 2021; Bao et al. 2022).

In addition to measuring the time delay for the integrated Hβ emission, we also investigated the possibility of constraining velocity-resolved time delays across the broad emission-line profile. Following the methods described in Section 3, we divided the Hβ profile into five velocity bins. We created a light curve for each bin and measured the time delay with respect to the continuum light curve.

In Figure 5 we show the time delays (τ_{cent}) measured as a function of velocity across the Hβ emission line. For comparison, the gray horizontal band marks the time delay and its uncertainties for the integrated emission line. A slight M-shaped pattern may be apparent in the time delays, reminiscent of that seen in the velocity-resolved time delays of the broad UV and optical emission lines in NGC 5548 (Rosa et al. 2015; Pei et al. 2017). Detailed analysis of the velocity-resolved signatures in NGC 5548 by Horne et al. (2021) revealed the M-shaped pattern to be the signature of an inclined Keplerian disk. IC 4329A has long been known (Disney 1973; Wilson & Penston 1979) as one of the few nearby AGNs to show clear double-peaked broad emission-line profiles. Storchi-Bergmann et al. (2017) suggest that double peaks in optical broad emission lines are more common among local Seyferts than generally recognized, and they include NGC 5548 among their sample. Double-peaked broad emission lines are often interpreted as indicating a disk-like BLR structure, so the potential similarities between the velocity-resolved responses of NGC 5548 and IC 4329A are perhaps unsurprising if they are both double-peaked AGNs. Nevertheless, while velocity-resolved time delays may provide hints, a more thorough analysis is required to constrain the details of the BLR geometry in IC 4329A.

4.4. CARAMEL Modeling

There are two independent approaches for analyzing velocity-resolved reverberation responses: as an ill-posed inverse problem or through forward modeling. The inverse approach attempts to extract the transfer function, which describes the time delay distribution as a function of velocity, directly from the data (Horne 1994; Skielboe et al. 2015; Anderson et al. 2021). Forward modeling, on the other hand,
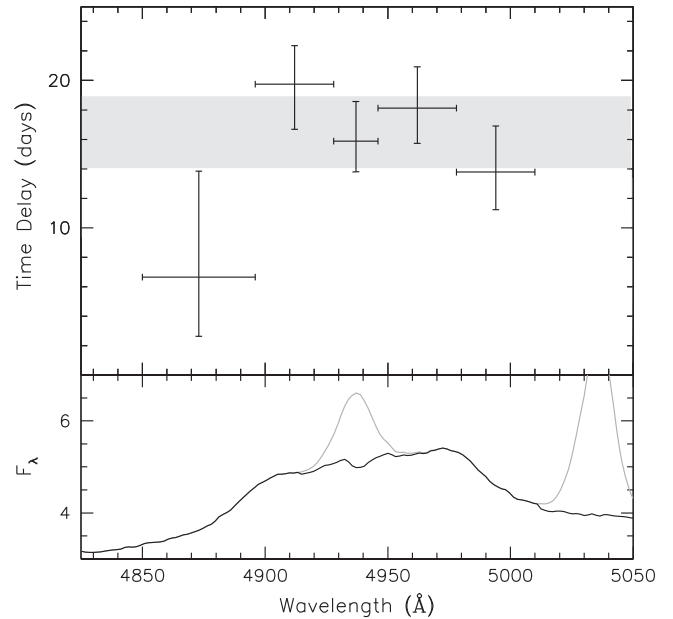

Figure 5. Velocity-resolved time delays (top) across the profile of the broad Hβ emission line (bottom). The narrow-line contributions to the mean spectrum are separately plotted in gray.

uses a framework of self-consistent models to explore the relevant parameter space and determine the set of models that best agree with the observations (Pancoast et al. 2011, 2014). Forward modeling has the advantage that the results are relatively simple to interpret, although it is limited by the flexibility and completeness of the models. The inverse approach, on the other hand, makes few initial assumptions and is generally more flexible, but produces results that may be difficult to interpret and generally rely on comparison with models.

We explored the possibility of constraining more details regarding the geometry and kinematics of the BLR in IC 4329A with the forward modeling code CARAMEL, following a similar approach to that we previously employed (Bentz et al. 2021b, 2022). In this case, most of the model parameters were not well constrained. Parameters with modest constraints included the black hole mass, $\log(M_{BH}/M_{\odot}) = 7.64^{+0.53}_{-0.25}$ or $M_{BH} = 4^{+10}_{-2} \times 10^{7}\ M_{\odot}$, and the average time delay, $\tau_{mean} = 13.6^{+9.2}_{-3.0}$ days, which agree with our results in Sections 3.1 and 4.2.

While the dynamics of the system were not constrained, there were weak constraints on some of the geometric parameters of the Hβ-emitting BLR (Figure 6), suggesting an average radius of $r_{mean} = 14.2^{+7.2}_{-3.7}$ lt-days, with a minimum
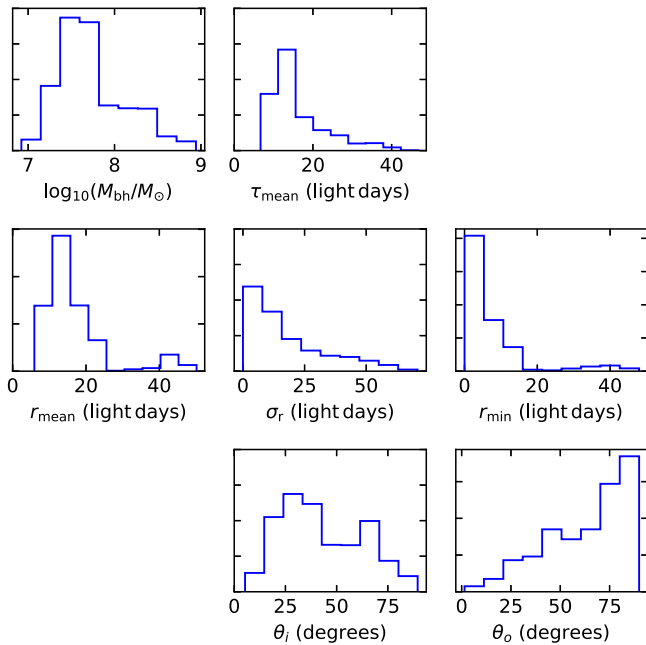
Figure 6. Posterior distributions of constraints on the Hβ-emitting BLR geometry.

radius of $r_{\min} = 3.1_{-2.5}^{+8.5}$ lt-days and a radial extent of $\sigma_r = 12.0_{-8.0}^{+22.5}$ lt-days.

Finally, modest constraints were derived for the inclination angle of the BLR relative to our line of sight, $\theta_i = 40.1_{-18.1}^{+26.6}$ deg, as well as the opening angle of the BLR, $\theta_o = 69.2_{-29.6}^{+15.3}$ deg, where $\theta_o = 0°$ is a thin disk and $\theta_o = 90°$ is a sphere. The inclination angle suggests that the AGN system and the galaxy disk are indeed misaligned by a significant amount ($\sim 25°$–$70°$). Furthermore, we note that the moderate inclination angle constrained by the models suggests that the value of $\langle f \rangle$ adopted in Section 4.2 is unlikely to be an underestimate for this particular AGN (see Williams et al. 2018).

Visualization of a random sampling of allowed BLR models included wide and puffy inclined annuli, filled inclined biconical structures, and inclined *hamburger buns* that resemble the intersection of a bicone with a shell. Thus, while these models demonstrate consistency with several previous results including those that we present above, they are limited in their ability to elucidate a more clear picture of the BLR in IC 4329A. Additional work will be required to determine whether these limitations are a result of the quality of the reverberation data, which are a bit noisy but do show a clear velocity-resolved response, or are instead due to a mismatch between the modeling assumptions in CARAMEL and the physical conditions of the BLR in IC 4329A.

5. Summary

We have presented a new reverberation mapping campaign focused on the AGN in the center of the edge-on spiral galaxy IC 4329A. With photometric and spectroscopic monitoring covering 2022 February–July, we were able to constrain the time delay of the broad Hβ and Hγ emission lines: $16.3_{-2.3}^{+2.6}$ days for Hβ and $16.0_{-2.6}^{+4.8}$ days for Hγ. He II $\lambda 4686$ also exhibited variability during these observations, but the time delay of $-0.6_{-3.9}^{+3.9}$ days is unresolved and consistent with zero days. The Hβ time delay is consistent with that expected from

the relationship between AGN luminosity and BLR radius for local Seyferts, after correcting the AGN luminosity for the expected ~ 2.4 mag of intrinsic extinction at 5100 Å.

Combining the time delay and width of Hβ, we find a black hole mass of $M_{\rm BH} = 6.8_{-1.1}^{+1.2} \times 10^7 M_\odot$ when adopting $\langle f \rangle = 4.8$. Based on the detection of velocity-resolved time delays across the Hβ broad-line profile, we carried out forward modeling of the reverberation data presented here. Many of the model parameters were relatively unconstrained, but the black hole mass and average Hβ time delay agreed with our measurements. Finally, the models suggest that the BLR is indeed severely misaligned with the disk of the host galaxy, in agreement with expectations from the unified model for AGNs given that broad emission lines are clearly visible in the spectrum of the nucleus of IC 4329A, and yet the galaxy is oriented edge-on to our line of sight.

ORCID iDs

Misty C. Bentz ⓘ https://orcid.org/0000-0002-2816-5398
Christopher A. Onken ⓘ https://orcid.org/0000-0003-0017-349X
Rachel Street ⓘ https://orcid.org/0000-0001-6279-0552
Monica Valluri ⓘ https://orcid.org/0000-0002-6257-2341

References

Abell, G. O., Corwin, H. G., Jr., & Olowin, R. P. 1989, ApJS, 70, 1
Alard, C. 2000, A&AS, 144, 363
Alard, C., & Lupton, R. H. 1998, ApJ, 503, 325
Anderson, M. D., Baron, F., & Bentz, M. C. 2021, MNRAS, 505, 2903
Antonucci, R. 1993, ARA&A, 31, 473
Bao, D.-W., Brotherton, M. S., Du, P., et al. 2022, ApJS, 262, 14
Batiste, M., Bentz, M. C., Raimundo, S. I., Vestergaard, M., & Onken, C. A. 2017, ApJL, 838, L10
Bentz, M. C., Denney, K. D., Grier, C. J., et al. 2013, ApJ, 767, 149
Bentz, M. C., & Katz, S. 2015, PASP, 127, 67
Bentz, M. C., Peterson, B. M., Netzer, H., Pogge, R. W., & Vestergaard, M. 2009a, ApJ, 697, 160
Bentz, M. C., Street, R., Onken, C. A., & Valluri, M. 2021a, ApJ, 906, 50
Bentz, M. C., Walsh, J. L., Barth, A. J., et al. 2008, ApJL, 689, L21
Bentz, M. C., Walsh, J. L., Barth, A. J., et al. 2009b, ApJ, 705, 199
Bentz, M. C., Williams, P. R., Street, R., et al. 2021b, ApJ, 920, 112
Bentz, M. C., Williams, P. R., & Treu, T. 2022, ApJ, 934, 168
Bernardi, M., Alonso, M. V., da Costa, L. N., et al. 2002, AJ, 123, 2990
Blandford, R. D., & McKee, C. F. 1982, ApJ, 255, 419
Brotherton, M. S., Du, P., Xiao, M., et al. 2020, ApJ, 905, 77
Brown, J. S., Kochanek, C. S., Holoien, T.-W.-S., et al. 2018, MNRAS, 473, 1130
Brown, T. M., Baliber, N., Bianco, F. B., et al. 2013, PASP, 125, 1031
Cackett, E. M., Bentz, M. C., & Kara, E. 2021, iSci, 24, 102557
Collin, S., Kawaguchi, T., Peterson, B. M., & Vestergaard, M. 2006, A&A, 456, 75
Czerny, B., Li, J., Loska, Z., & Szczerba, R. 2004, MNRAS, 348, L54
Denney, K. D., Peterson, B. M., Pogge, R. W., et al. 2009, ApJL, 704, L80

Disney, M. J. 1973, ApJL, 181, L55
Fausnaugh, M. M., Denney, K. D., Barth, A. J., et al. 2016, ApJ, 821, 56
Fausnaugh, M. M., Grier, C. J., Bentz, M. C., et al. 2017, ApJ, 840, 97
Gaskell, C. M., & Peterson, B. M. 1987, ApJS, 65, 1
Gaskell, C. M., & Sparke, L. S. 1986, ApJ, 305, 175
Graham, A. W., Onken, C. A., Athanassoula, E., & Combes, F. 2011, MNRAS, 412, 2211
Grier, C. J., Martini, P., Watson, L. C., et al. 2013a, ApJ, 773, 90
Grier, C. J., Pancoast, A., Barth, A. J., et al. 2017, ApJ, 849, 146
Grier, C. J., Peterson, B. M., Horne, K., et al. 2013b, ApJ, 764, 47
Hamuy, M., Suntzeff, N. B., Heathcote, S. R., et al. 1994, PASP, 106, 566
Hamuy, M., Walker, A. R., Suntzeff, N. B., et al. 1992, PASP, 104, 533
Hartman, J. D., Bakos, G., Stanek, K. Z., & Noyes, R. W. 2004, AJ, 128, 1761
Hartman, J. D., Stanek, K. Z., Gaudi, B. S., Holman, M. J., & McLeod, B. A. 2005, AJ, 130, 2241
Henden, A., & Munari, U. 2014, CoSka, 43, 518
Holoien, T. W. S., Kochanek, C. S., Prieto, J. L., et al. 2016, MNRAS, 463, 3813
Horne, K. 1994, in ASP Conf. Ser. 69, Reverberation Mapping of the Broad-Line Region in Active Galactic Nuclei, ed. P. M. Gondhalekar, K. Horne, & B. M. Peterson (San Francisco, CA: ASP), 23
Horne, K., Rosa, G. D., Peterson, B. M., et al. 2021, ApJ, 907, 76
Hudson, M. J., Lucey, J. R., Smith, R. J., Schlegel, D. J., & Davies, R. L. 2001, MNRAS, 327, 265
King, A. R., & Pringle, J. E. 2007, MNRAS, 377, L25
Lousto, C. O., Healy, J., & Nakano, H. 2016, PhRvD, 93, 044031
Malin, D. F., & Carter, D. 1983, ApJ, 274, 534
Markowitz, A. 2009, ApJ, 698, 1740
McCully, C., Volgenau, N. H., Harbeck, D.-R., et al. 2018, Proc. SPIE, 10707, 107070K
McHardy, I. M., Koerding, E., Knigge, C., Uttley, P., & Fender, R. P. 2006, Natur, 444, 730
Mehdipour, M., & Costantini, E. 2018, A&A, 619, A20
Melinder, J., Mattila, S., Ostlin, G., Mencia Trinchant, L., & Fransson, C. 2008, A&A, 490, 419
Miknaitis, G., Pignata, G., Rest, A., et al. 2007, ApJ, 666, 674
Morris, S. L., & Ward, M. J. 1988, MNRAS, 230, 639
Nagar, N. M., & Wilson, A. S. 1999, ApJ, 516, 97

Oknyansky, V. L., Brotherton, M. S., Tsygankov, S. S., et al. 2021, MNRAS, 505, 1029
Onken, C. A., Ferrarese, L., Merritt, D., et al. 2004, ApJ, 615, 645
Pancoast, A., Brewer, B. J., & Treu, T. 2011, ApJ, 730, 139
Pancoast, A., Brewer, B. J., & Treu, T. 2014, MNRAS, 445, 3055
Park, D., Kelly, B. C., Woo, J.-H., & Treu, T. 2012, ApJS, 203, 6
Pei, L., Fausnaugh, M. M., Barth, A. J., et al. 2017, ApJ, 837, 131
Peng, C. Y., Ho, L. C., Impey, C. D., & Rix, H.-W. 2002, AJ, 124, 266
Peng, C. Y., Ho, L. C., Impey, C. D., & Rix, H.-W. 2010, AJ, 139, 2097
Peterson, B. M., Denney, K. D., De Rosa, G., et al. 2013, ApJ, 779, 109
Peterson, B. M., Ferrarese, L., Gilbert, K. M., et al. 2004, ApJ, 613, 682
Peterson, B. M., Wanders, I., Horne, K., et al. 1998, PASP, 110, 660
Ponti, G., Papadakis, I., Bianchi, S., et al. 2012, A&A, 542, A83
Read, A. M., & Pietsch, W. 1998, A&A, 336, 855
Riess, A. G., Nugent, P. E., Gilliland, R. L., et al. 2001, ApJ, 560, 49
Rosa, G. D., Peterson, B. M., Ely, J., et al. 2015, ApJ, 806, 128
Schlafly, E. F., & Finkbeiner, D. P. 2011, ApJ, 737, 103
Schmitt, H. R., Kinney, A. L., Storchi-Bergmann, T., & Antonucci, R. 1997, ApJ, 477, 623
Siverd, R. J., Beatty, T. G., Pepper, J., et al. 2012, ApJ, 761, 123
Skielboe, A., Pancoast, A., Treu, T., et al. 2015, MNRAS, 454, 144
Stahl, B. E., de Jaeger, T., Boruah, S. S., et al. 2021, MNRAS, 505, 2349
Storchi-Bergmann, T., Schimoia, J. S., Peterson, B. M., et al. 2017, ApJ, 835, 236
Tremaine, S., Gebhardt, K., Bender, R., et al. 2002, ApJ, 574, 740
Tully, R. B., Rizzi, L., Shaya, E. J., et al. 2009, AJ, 138, 323
Udalski, A., Szymanski, M. K., Soszynski, I., & Poleski, R. 2008, AcA, 58, 69
Udalski, A., Szymański, M. K., & Szymański, G. 2015, AcA, 65, 1
van Groningen, E., & Wanders, I. 1992, PASP, 104, 700
White, R. J., & Peterson, B. M. 1994, PASP, 106, 879
Whittle, M. 1992, ApJS, 79, 49
Williams, P. R., Pancoast, A., Treu, T., et al. 2018, ApJ, 866, 75
Wilson, A. S., & Penston, M. V. 1979, ApJ, 232, 389
Winge, C., Peterson, B. M., Pastoriza, M. G., & Storchi-Bergmann, T. 1996, ApJ, 469, 648
Wolstencroft, R. D., Done, C. J., Scarrott, S. M., & Scarrott, R. M. J. 1995, MNRAS, 276, 460
Zebrun, K., Soszynski, I., & Wozniak, P. R. 2001, AcA, 51, 303
Zu, Y., Kochanek, C. S., & Peterson, B. M. 2011, ApJ, 735, 80